DEVELOPMENT OF A HYDROXYAPATITE REINFORCED, LOAD-BEARING SCAFFOLD FOR BONE REGENERATION

By:

Pushpendra Pankaj Patel

A thesis submitted to the

Graduate School of New Brunswick

and

The Graduate School of Biomedical Sciences

Rutgers, The State University of New Jersey

In partial fulfillment of the requirements

For the degree of

Master of Science

Graduate Program in Biomedical Engineering

Written under the direction of

Dr. Joseph W. Freeman

And approved by

_____

_____

_____

New Brunswick, New Jersey

January 2017

ABSTRACT OF THE THESIS

Development of a Hydroxyapatite Reinforced, Load-Bearing Scaffold for Bone Regeneration

By: Pushpendra P. Patel

Thesis Advisor: Dr. Joseph W. Freeman

With over 500,000 bone grafting procedures performed annually in the United States alone, the advancement of bone tissue regeneration has come to the forefront of medical research [1,2]. While native bone tissue does possess a limited ability to repair itself, surgical intervention is required for injuries with critical sized defects. Autografts and allografts are the accepted gold standard treatment options; however, their application is limited by donor site morbidity and disease transmission, respectively [2]. Although various tissue-engineered approaches have been explored to develop a viable synthetic bone graft substitute, a major challenge has been achieving a load-bearing design that can appropriately mimic the mechanical properties of native bone tissue [1]. To address the issue, this study focuses on using hydroxyapatite (HAp)—a calcium phosphate derivative similar to the inorganic mineral found in bone—to develop a structurally reinforced scaffold, which exhibits the mechanical properties of native whole bone. HAp packed into a cylindrical framework was processed under varying conditions (sintering time, sintering temperature, packing pressure, and hydroxyapatite grain size) to maximize its mechanical properties. The resulting HAp columns were further tested in a 6-week degradation study, to determine the physical and mechanical response of the columns under biological conditions. The cellular response of sintered HAp columns was

determined using murine preosteoblast cell line MC3T3-E1. Cell viability, metabolic activity, and morphology were studied over a one-week period. To structurally reinforce a composite trabecular and cortical bone scaffold that was previously developed in the MoTR Lab [1], Finite Element Analysis (FEA) was used to determine the columns' geometric configuration and arrangement within the scaffold. Preliminary results indicate that the incorporation of a mechanically enhanced HAp structural support system is a promising step towards developing one of the first load-bearing bone scaffolds that can also promote osteoblastic and vascular differentiation.

ACKNOLEDGEMENTS

I would like to thank my advisor, Dr. Joseph W. Freeman, for his guidance throughout the course of my undergraduate and graduate studies. Under his tutelage, I was able to successfully see the completion of this project. I would also like to thank Brittany Taylor, Christine Sahyoun, Samarth Patel, Ashley Mont and all other members of the MoTR Lab for their guidance throughout the course of this project. In addition, I would like to thank my committee members: Dr. Michael Dunn and Dr. Ronke Olabisi.

Some data from this thesis has been previously published in the IEEE Xplore® Digital Library and is the original work of M.S. candidate, Pushpendra P. Patel

P. Patel, B. Taylor, & J. Freeman. (2014). Mechanical enhancement of a tissue-engineered scaffold for bone regeneration. 2014 40th Annual Northeast Bioengineering Conference (NEBEC), pp. 1-2.

Table of Contents

List of Figures

List of Tables

CHAPTER 1 – Introduction

1.1 Bone Structure and Function

Bone is a connective tissue comprised of a dynamic network of organic and inorganic material. It performs a variety of functions in the body ranging from mineral homeostasis to providing a structural framework for the musculoskeletal system [2]. Native bone is anisotropic and has a hierarchical organization that is fundamental to understanding its properties and function. On the macro-level, bone can be categorized into cortical (compact) bone and trabecular (cancellous) bone [3,5]. Densely packed cortical tissue—a fundamental component of long bones such as the femur—plays an important role in bone's load-bearing function. It is found in layers, surrounding the more porous trabecular bone, which is prominently found at the ends of long bones [3].

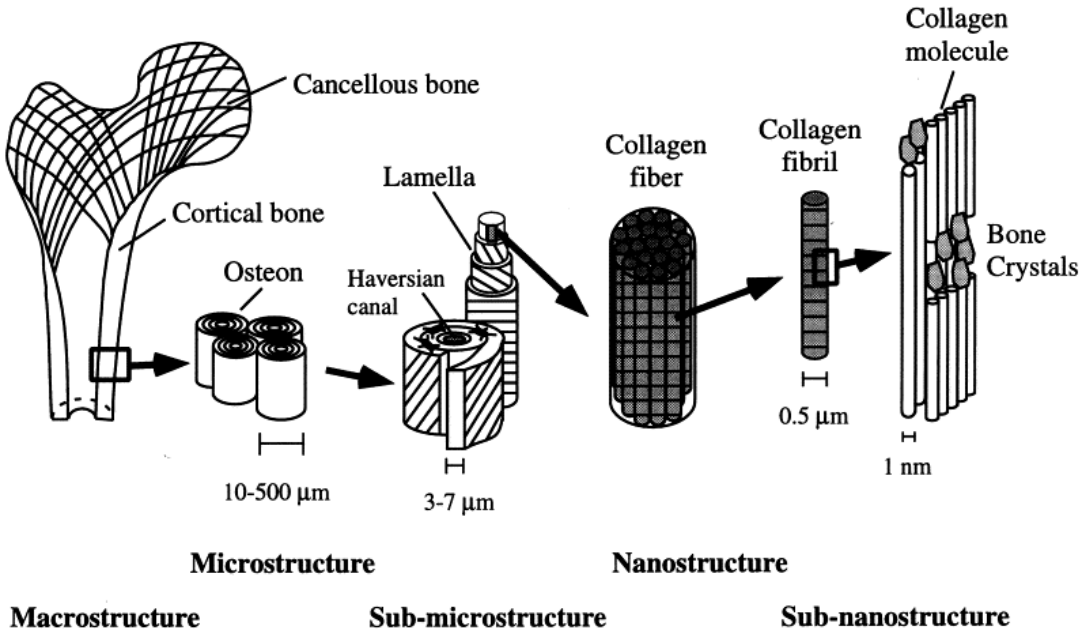

Figure 1: *Hierarchical structure of native bone tissue [3]*

On the micro-scale, bone is a biphasic matrix composed of organic type-I collagen fibers and inorganic calcium phosphate nanocrystals. Calcium phosphate provides mechanical stiffness (ability to resist deformation), while the collagen provides elasticity and mechanical toughness (ability to absorb energy) [2,5]. These basic bone materials are organized into planar structures called lamellae, which have a thickness between 3 to 7 um. Within an individual lamella, collagen is bundled together as parallel fibers along its surface [4,5].

In cortical bone, mineralized lamella layers are seen in concentric arrangements, forming a hollow cylindrical structure known as an osteon—the basic functional unit of cortical bone [3]. Osteons have a diameter ranging from 200 to 250 μm and are oriented along the longitudinal axis of long bones. These cylindrical structures contain a hollow central canal—called the Haversian canal—which houses blood and lymphatic vessels and nerve fibers [2,4,5]. These 50-90 μm canals are necessary to ensure proper nutrient diffusion throughout the densely mineralized tissue [4,5].

Trabecular bone differs from cortical bone in its architecture and porosity. While cortical bone can have a porosity between 5-30%, the porosity of trabecular bone ranges from 30-90% [2,3,4,5]. The high porosity is necessary to allow trabecular bone to house red bone barrow, which is responsible for the generation of new blood cells [2,3,6]. The porosity of trabecular bone can be attributed to its mesh-like lattice, which is called trabeculae. Trabeculae have characteristic rod and plate structures that connect the lattice framework.

These interconnections within trabeculae are periodically remodeled along the direction of mechanical stresses to meet the demands of physiological stimuli [2,3,7].

1.2 Bone Composition

Healthy bone is comprised of 50-70% calcium phosphate mineral, 20-40% type-I collagen, and 5-10% water [4,8]. Additionally, there are small quantities of type-III and type-IV collagen, proteoglycans, and non-collagenous proteins that help bind various layers of the mineralized matrix [9]. The mineral phase of bone is found in the form of calcium phosphate apatite. The platelet-shaped apatite crystals nucleate from periodic gaps within the collagen fibril structure, forming a discontinuous mineral phase [3,5,10]. Bone apatite mineral is similar in composition to commercially available hydroxyapatite ($Ca_{10}(PO_4)_6(OH)_2$) [10]. Although hydroxyapatite is the most stable calcium phosphate apatite, spectroscopy analysis of bone apatite has shown several impurities in the form of ionic substitutions [10,11]. While the exact pattern of impurity substitution is not known, notable differences include the lack of a hydroxyl moiety and the presence of carbonate, chloride, fluoride, and magnesium ions [10].

1.3 Bone Mechanical Properties

The mechanical properties of native bone tissue are dependent on a multitude of factors including testing parameters, age of the tissue, and tissue quality [7, 12]. During initial loading, bone exhibits a linear region on the stress strain curve. The slope of the linear region is known as the Young's Modulus, which measures an object's stiffness. Elastic deformation is observed only in the linear region, where loading is below the yield

strength. Cortical and trabecular bone exhibit distinct mechanical properties due to differences in their primary structure. Trabecular bone is known to have a compressive modulus ranging from 10-2000 MPa and an ultimate compressive strength of approximately 50 MPa [12]. In the longitudinal direction, cortical bone has an average compressive modulus of 17,000 MPa and an ultimate compressive strength of 193 MPa [12]. While cortical bone has a larger modulus, allowing it to withstand larger mechanical stresses, trabecular bone has a greater capacity to absorb energy upon loading [11].

Bone also exhibits viscoelasticity, evidenced by differences in mechanical behavior that depend on the strain rate (Figure 2). Figure 2 shows that as the strain rate increases, bone exhibits a larger modulus. However, the modulus is not significantly affected during normal physiological loading [12].

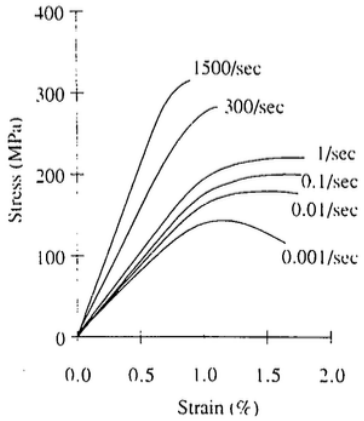

Figure 2: *Mechanical behavior of bone as a function of strain rate. [11]*

Physiological loading of bones such as the tibia is complex and results in a combination of stresses including tension, compression, bending, torsion, and shear. Testing protocols

for bone are complicated by its anisotropic characteristics, which accounts for differences in tensile and compressive mechanical properties [7,12]. In addition, transverse and longitudinal loading accounts for differences in the loading profile. Bone is strongest under a longitudinal uniaxial compressive load [12].

1.4 Fractures and Defects

Bone fractures are one of the most common orthopaedic injuries, with up to 7.9 million fractures reported annually in the United States alone [13,14]. Nearly 10% of these cases can result in complications resulting in delayed healing [13,15]. Fractures can result from abnormal mechanical loading in healthy bone tissue or normal physiological loading in abnormal bone tissue [16]. In the case of severe trauma, a fracture can occur if the energy of an impact exceeds the energy that bone is able to absorb and dissipate [12]. One of the most common types of fracture is called the fatigue fracture, which occurs from repeated mechanical loading with magnitudes below the load-bearing capacity of bone [16]. Insufficiency fractures occur when normal physiological loading results in the failure of deficient (i.e. osteoporotic) bone. These types of fractures are a result of long term accumulated loading [16]. It is estimated that nearly 1.5 million people suffer from insufficiency fractures as a result of bone disease [17].

1.5 Current Treatments

Treatment of orthopaedic bone fractures involves realignment and fixation of the fragmented ends to allow for proper bone tissue regeneration at the site of injury. While many cases can be remedied by non-invasive fixation devices such as a cast, some

injuries require fixation by bone-plates and screws to facilitate healing [18]. If bone healing continues to be deficient after fixation, grafts are used to fill voids, where they serve as a matrix to stimulate new tissue ingrowth and promote healing between disjointed ends of the bone [19]. The benchmark treatment uses an autologous graft, where bone is harvested from the patient's own body [1,2,19,20]. Alternative sources of biological grafts include allografts, which are harvested from cadaver donated tissue [19]. With the supply of biological grafts being severely limited, synthetic bone graft substitutes are being increasingly studied [20].

For success in clinical practice, all grafts should meet certain characteristics that are required to support the generation of new bone tissue. Successful grafts should exhibit a combination of osteoconduction, osteoinduction, and osteogenesis [19,20,21]. Osteoconduction refers to a graft's ability serve as a scaffold and support new bone ingrowth, generated by osteoblasts from surrounding native bone tissue. Osteoinduction occurs when the graft is able to recruit progenitor cells and promote osteoblastic differentiation. Osteoinductive cues include growth factors such as bone morphogenic protein (BMP). Osteogenetic grafts have their own supply of osteoblasts that generate bone tissue, which supplements osteoconduction from surrounding bone [19,21]. In addition, grafts must support vascularization and should have appropriate mechanical strength for injuries at load-bearing sites [1,2].

1.5.1 Autografts

Autologous sources of bone grafts are considered the gold standard in grafting procedures because of their enhanced ability to support osteoconduction and osteoinduction during new bone formation [1,2,19,20]. Additionally, autografts are the only graft source that can support osteogenesis, because they have their own supply of osteoblasts. Autologous grafts can include trabecular bone, cortical bone, or a composite of the two types [19]. The most common harvesting site for autografts is the iliac crest, located in the pelvis [19,21,22]. Less prominent donor sites include the distal radius, proximal tibia, and the ribs [22].

Although autografts are optimal for bone regeneration at the site of injury, they require a secondary surgery that can lead to increased complications, including donor site morbidity and prolonged recovery times. Autologous harvesting is particularly limited for patients with malignant diseases and older patients who cannot afford the risk of an additional surgery [19]. Regardless of age, there is a limit to the amount of graft tissue that can be safely harvested; morbidity rates as high as 49% have been reported for grafts harvested from the iliac crest [2,24] In addition to the limited supply of autologous tissue, harvesting procedures can lead to increased pain, nerve damage, formation of hematoma, etc. [19,24]. Nevertheless, autografts remain the gold standards for its long term success rate.

1.5.2 Allografts

Although autologous tissue remains the gold standard for bone grafting procedures, allografts are the most commonly grafted bone tissue [19,25]. Improvements to sterilization techniques have resulted in an increased supply of transplantable cadaver tissue, allowing allografts to be used in nearly one-third of all bone grafting procedures in the United States [25]. However, allografts still carry the risk of disease transmission and immunogenic response [21,26]. In clinical practice, there is variation in their success rates because allografts do not possess osteogenetic capabilities and they have exhibited inferior osteoconductivity and osteoinductivity compared to autografts [19]. In addition to these limitations, allografts experience up to a 50% loss in mechanical properties, which contributes to an *in vivo* failure rate as high as 60%, 10 years after transplantation [27]. While sterilization techniques play a factor in the loss of both mechanical and biological properties of allografts, the cause of long term failure requires further investigation [19,21,28]. Allograft procedures are still commonly carried out in the clinic because they do not require a secondary surgery at the harvesting site.

1.5.3 Xenografts

Xenografts are harvested from animal tissue (most commonly bovine) and are associated with many of the same concerns as allografts [29]. Xenografts have been widely studied because they offer an alternative graft source to compensate for the short supply of autografts and allografts [19,29]. To address biocompatibility issues, xenografts are heavily processed to remove all proteins and lipids [30]. The inorganic matrix that results from the processing and sterilization of xenografts exhibits minimal resorption, which

can compromise healing at the site of injury [29]. Although limited, there are commercially available xenograft substitutes such as the deproteinized bovine Straumann® XenoGraft.

1.5.4 Synthetic Bone Graft Substitutes

With the growing demand for bone grafting procedures, synthetic graft substitutes are being explored to compensate for the limited supply of biological grafts. The bone graft substitute market generates approximately $1 billion USD annually and is expected to achieve an annual market growth nearing 10% [31]. Synthetic graft substitutes avoid the risk of disease transmission and secondary surgery and can be readily reproduced to keep up with growing demands [20,29]. A variety of materials have been proposed for synthetic substitutes including polymers, ceramics, and metals. More recently, there has been an emphasis on resorbable biomaterials, which are eventually replaced by new bone tissue over time [31].

For hard tissues such as bone, bioceramics have been one of the most widely studied materials and have been used in orthopedics since the 1980's [32]. Calcium phosphates and silicon based bioactive glass are two of the most commonly proposed ceramics for bone tissue regeneration. Bioactive glass (also known as Bioglass®) has gained interest predominantly for its ability to integrate directly with native bone tissue. Primarily composed of silicone dioxide, bioactive glass is a hard substance that undergoes a multi-step process to form bone-like apatite mineral, which allows it to bind directly to native tissue [32,33]. Although the biocompatibility and biodegradation of Bioglass® has been

established, certain mechanical concerns need to be addressed. The application of Bioglass® grafts in load-bearing is still limited because of its inability to meet the mechanical strength of native bone [34]. While some studies have altered the fabrication technique of Bioglass® to increase its mechanical properties, the graft still suffers from brittleness, which limits its resistance to fractures [33-34].

Calcium phosphates are a promising category for bone regeneration because of their similarity to native bone. The most prominent calcium phosphate materials for bone tissue engineering are hydroxyapatite (HAp) and β-tricalcium phosphate (β-TCP) [20,33,35]. Although β-TCP has a long track record of osteoconductivity and biocompatibility, it exhibits a rapid resorption that exceeds the rate at which new bone can be generated [36]. This limits the use of β-TCP as a standalone material in bone regeneration technology. HAp displays more favorable mechanics and has shown to have limited biodegradation, allowing it to withstand compressive loads throughout the process of new bone generation [33,35]. HAp exhibits structural similarity to the calcium phosphate mineral found in bone apatite and can act as nucleation sites for the formation of new bone, forming a highly integrated layer with the surrounding native bone tissue [10,20,37]. Composite ceramics consisting of varying ratios of HAp and β-TCP have been studied in an effort to control mechanical properties and biodegradation rates [36]. A limitation of ceramic based bone regeneration remains the brittleness and low fracture toughness of materials such as HAp [5,37]. Composites of ductile polymers such as poly(lactic acid) and hydroxyapatite can help optimize the material and biological properties of these materials [37].

1.6 Project Aims

The aim of this project is to structurally reinforce a previously developed composite trabecular and cortical biomimetic bone scaffold using hydroxyapatite (HAp). First, sintered HAp was mechanically characterized and a fabrication protocol was established. The mechanically enhanced HAp columns were subject to degradation analysis to assess their mechanical response under biological conditions. The columns' *in vivo* biocompatibility was assessed and cellular morphology was observed. The columns were scaled and arranged in the composite scaffold based on Finite Element Analysis (FEA). It was hypothesized that reinforcing the polymeric scaffold with sintered HAp columns would contribute to the development of one of the first load-bearing bone scaffolds that can also promote vascularization and osteoblastic differentiation.

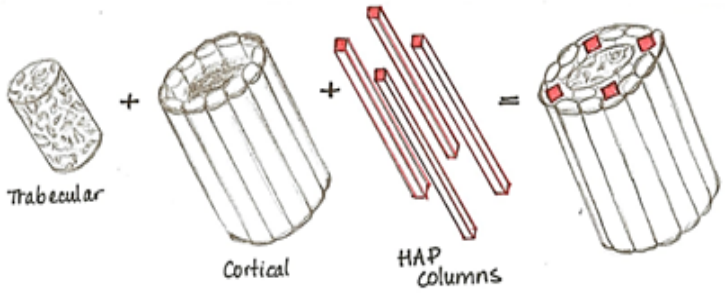

Figure 3: *Schematic of proposed composite 3-D scaffold with HAp columns.*

CHAPTER 2 – Fabrication and Characterization of Hydroxyapatite Columns

The aim of this project was to mechanically reinforce a previously developed polymeric bone scaffold by developing a structural support system using synthetic hydroxyapatite (HAp). HAp was processed to develop a bioceramic column capable of withstanding large compressive loads. Different types of HAp powders and their processing parameters were analyzed to achieve maximum compressive properties, which were assessed via mechanical testing on an Instron 5869. A protocol for HAp column fabrication was developed. The columns' microstructure was assessed using SEM imaging. The degradation of the columns what characterized to determine the mechanical response of the HAp columns under biological conditions. The columns were seeded with pre-osteoblasts to determine cell viability and morphology.

2.1 Materials and Methods

In this study, two types of hydroxyapatite powders were assessed—reagent grade synthetic hydroxyapatite (with micro-sized particles) and hydroxyapatite nanopowder (particle size <200 nm). Both were purchased from Sigma Aldrich. The HAp was packed into a cylindrical framework under high and low pressure conditions and sintered in a muffled furnace at varying times and temperatures.

2.1.1 Fabrication of HAp Columns

Approximately one gram of hydroxyapatite powder was packed in a cylindrical mold with a diameter of 6 mm and a height of 10 mm. To coagulate the powder, 0.1 mL

deionized water was added, dropwise. A minimal amount of dI water was used to minimize the formation of micro cracks caused by vaporization during the sintering process. An Instron mechanical testing system (Model 5869, Norwood, MA) was used to apply a constant packing pressure of 44 MPa for 10 minutes. The columns were sintered at 1200°C for 3 and 5 hours in a ThermoScientific EuroTherm 2116 Benchtop Muffle furnace.

The effects of packing pressure, sintering time, and hydroxyapatite particle size were assessed. Hand packed columns, fabricated without the application of pressure were compared to columns that were packed under 44 MPa of pressure. Both of these groups were sintered at 1200°C for 5 hours. To compare the effect of sintering time, columns packed using 44 MPa of pressure were sintered at 1200°C for 3 and 5 hours. The effect of particle size on the mechanical properties of the final product was assessed using hydroxyapatite nanopowder and reagent grade synthetic hydroxyapatite. They were both packed at 44 MPa and sintered at 1200°C for 5 hours. The compressive modulus of all samples were compared so that processing conditions could be modified to maximize mechanical properties and a final fabrication protocol could be determined.

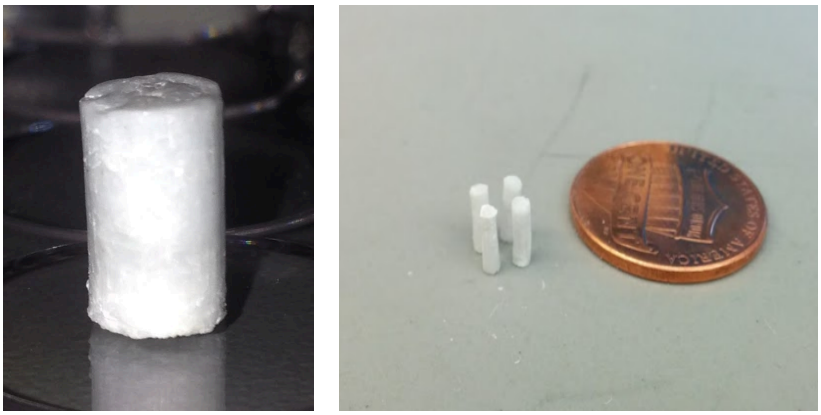

Figure 4: *Sintered HAp columns packed under 44 MPa of pressure and sintered at 1200C for 5 hours. Columns scaled and incorporated into composite scaffold shown on the right.*

2.1.2 Mechanical Testing

After the sintered bioceramic columns were cooled to room temperature, they were subject to compressive testing, which was performed on an Instron 5869 mechanical testing system, using a 50 kN load cell. All columns were dry at the time of testing. To ensure uniform loading across the cross sectional area of the ceramic columns, surface abnormalities on the top and bottom surfaces of the cylindrical samples were carefully polished flat using sandpaper. The samples underwent compressive testing at a rate of 1 mm/min. For each sample, a stress-strain curve was generated from the load-extension data obtained from the Instron. The ultimate compressive strength and the Young's Modulus was calculated.

2.1.3 HAp Surface Characterization Using Scanning Electron Microscopy

All HAp samples were placed in a desiccator for 24 hours prior to imaging. The dried samples were sputter coated with a 10 nm layer of gold. Columns were imaged with a Zeiss Sigma Field Emission SEM with Oxford INCA PentaFETx3 EDS system (Model 8100)

2.1.4 Degradation Study

After analysis of the mechanical data, a fabrication protocol was determined. The degradation profile of HAp columns packed under 44 MPa of pressure and sintered at 1200°C for 5 hours was studied. During this study, a custom Instron program was created, which periodically lowered the load cell to compensate for the drop in applied pressure when the HAp particles rearrange to dissipate energy. This better maintained a constant packing pressure of 44 MPa throughout the 10-minute duration. HAp nanopowder particles rearrange in order to dissipate some of the energy so The weight and dimensions of each column was documented prior to the study. Samples were individually placed in separate vials and submerged in 5 mL of phosphate buffered saline (PBS). The vials were placed in a Boekel Scientific Shaking Waterbath set at 37°C. To simulate physiological movement, samples placed in the waterbath were subject to orbital rotation and a constant rate of 70 RPM. Using this setup, degradation of the columns was assessed at weeks 4 and 6. The columns were removed from the PBS solution and dried in a desiccator for 24 hours. The weight and dimensions of each column were compared before and after the degradation period. Using the Instron 5869, samples were then

subjected to the same testing protocol described during initial mechanical characterization.

2.1.5 Scaffold Sterilization and Preparation

HAp columns with a height of 2 mm and a diameter of 4 mm were used to study *in vitro* biocompatibility. The columns were packed under 44 MPa of pressure and sintered at 1200°C for 5 hours. The top and bottom surfaces were polished flat using sandpaper. Multiple sterilization steps were taken to prepare the columns for cell seeding. First, the HAp columns were autoclaved. Next, they were brought into a SteriGuard class II sterile hood where each column was attached to the bottom of a 24-well plate using a sterile adhesive. 2 mL of 70% ethanol was added to each well, completely submerging the samples for 30 minutes. After the ethanol was removed, the columns were exposed to UV light for 30 minutes. The well plate was flipped and the bottom of the samples were exposed to UV light for an additional 30 minutes. The columns were washed with sterile PBS 3 times to remove any trace of ethanol. Finally, each column was soaked overnight in 1 mL of Alpha Minimum Essential Medium (α-MEM) (Gibco by Life Technologies, Carlsbad, Ca), supplemented with 10% fetal bovine serum (FBS) and 1% penicillin and streptomyocin (P/S). The soaking step was performed to enhance cell adhesion onto the HAp columns.

2.1.6 Cell Seeding

For this cell study, murine preosteoblast cell line MC3T3-E1 subclone 4 was purchased (ATCC®, CRL-2593™). The passage 1 cells were expanded using α-MEM, supplemented

with 10% fetal bovine serum (FBS) and 1% penicillin and streptomyocin (P/S). The α-MEM used during the expansion procedure did not contain ascorbic acid in order to maintain the cells' preosteoblastic properties. Exposure to ascorbic acid is known to promote MC3T3-E1 cells to undergo osteoblastic differentiation. The cells were grown at 37°C in a humidified incubator (5% CO_2) until they reached about 80% confluency. Media was replenished every other day during expansion.

As the cells became confluent, the HAp columns were sterilized as described in the previous section. The media soaked columns were washed once with sterile PBS. Expanded MC3T3-EI cells were detached from the culture flask using TrypLE™ Express and counted on a hemocytometer. Cells were seeded directly onto the top surface of the columns at a density of 10,000 cells/cm^2 (19,800 cells/well). 1 mL of α-MEM (supplemented with 10% FBS and 1% P/S) was added to each well, fully submerging the samples. Standard α-MEM containing ascorbic acid was used during cell seeding and for the remainder of this study. MC3T3-E1 cells were also seeded onto empty wells at a density of 10,000 cells/cm^2 to serve as a control. The cellular behavior was studied at days 1, 3, and 7. A sample size of $n \geq 4$ was used for each group. Media was replenished on days 2, 4, and 6.

2.1.7 Measuring Cell Viability Using PrestoBlue®

PrestoBlue® Cell Viability Reagent (Invitrogen, Frederick, MD) was used to quantify cellular proliferation. PrestoBlue® contains resazurin—a redox indicator that changes from dark blue to red, when reduced. Metabolically active cells create a reducing

environment that causes a rapid shift in fluorescence, which can be detected using a microplate reader. The assay depends on cellular metabolic activity, therefore, serving as an indirect measure of viability. All steps of the assay were carried out in a dark room to prevent background light interference, preserving assay sensitivity. First, a 1:10 dilution of the PrestoBlue® reagent in α-MEM cell culture media was prepared. 1 mL of the 1:10 PrestoBlue® solution was added to each well. To eliminate light exposure, the well plate was wrapped in aluminum foil and transferred to an incubator (37°C, 5% CO_2). After a 1-hour incubation period, 200 uL triplicates were taken from each well and transferred to a 96-well plate. 200 uL triplicates of the original 1:10 solution of PrestoBlue® was included as a control, allowing comparison of relative fluorescence between groups. Fluorescence absorbance was measured at 570 nm using a Tecan M200 Microplate Reader. Cell viability was measured using PrestoBlue® on days 1, 3, and 7.

2.1.8 Phalloidin and NucBlue® Immunostaining

After cell viability data was obtained, samples were washed with PBS two times. Cells were fixed by adding 1 mL of a 3.7% solution of paraformaldehyde to each well. After a 10-minute incubation period, the paraformaldehyde was aspirated and the wells were washed with 1 mL of PBS solution 3 times. Following each rehydration step, the plate was left to incubate at room temperature for 15 minutes. After the final wash step, 1 mL of 0.5% Triton X-100 (TX100) solution was added and incubated for 15 minutes. TX100 is a nonionic surfactant that promotes irreversible permeabilization of cell membranes in order to allow fluorescence stain molecules to penetrate the cell membrane. Following two additional wash steps, a 1% solution of bovine serum albumin (BSA) was added to

minimize non-specific binding of stain molecules. After a 30-minute incubation period, the BSA was washed with 1 mL of PBS. 1mL of a 1:100 solution of fluorescin phalloidin (Molecular Probes® F432 by Life Technologies™) was incubated in each well for 20 minutes. Phalloidin green is a peptide molecule that binds to F-actin, which is found primarily on the cytoskeleton. NucBlue® Live Ready Probes® Reagent (Molecular Probes® by Life Technologies™) has a high affinity for DNA and was used to stain cell nuclei. A 2 drops/mL solution of NucBlue® was prepared and incubated in each well for 10 minutes. After washing with PBS, the samples were ready for imaging on a fluorescence microscope. All staining steps were carried out in a dark room to minimize light exposure.

2.1.9 Fluorescence Microscopy

On days 1, 3, and 7, fluorescently labeled cells were imaged using a Leica Microsystems DMI 4000 B fluorescence microscope. HAp columns were detached from the well plate and transferred to a new plate prior to imaging. The columns were flipped upside down so that cell attachment and morphology could be observed on the top surface. Images of the phalloidin stained cytoskeleton was obtained at 496 nm. Images of cell nuclei stained with NucBlue® Live Ready Probes® Reagent was obtained at 360nm.

2.1.10 Visualization of Cell Morphology Using Scanning Electron Microscopy

MC3T3-E1 cells seeded onto HAp columns were further visualized using the Zeiss Sigma Field Emission SEM with Oxford INCA PentaFETx3 EDS system (Model 8100). Cells seeded on the columns were fixed as described during the staining protocol.

Samples were frozen for 24 hours in a -80°C freezer, then lyophilized overnight. The freeze-dried samples were sputter coated with a 10 nm layer of gold prior to imaging.

2.1.11 Determining the Arrangement of HAp Columns within the Scaffold

Finite Element Analysis (FEA) was used to determine the dimensions and arrangement of the HAp columns in the composite trabecular and cortical bone scaffold. Multiple three-dimensional scaffolds were designed using Solidworks software (Figure 5).

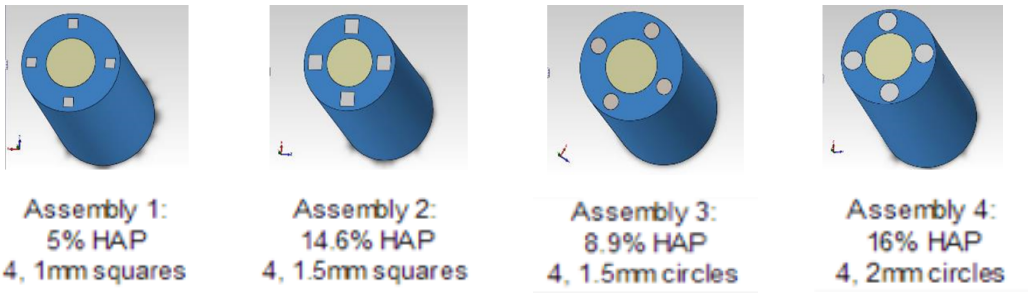

Figure 5: *Scaffold assemblies tested using FEA to determine optimal size and shape of the HAp columns. HAp is depicted in grey on the periphery of the circular cross section.*

Using a fixed geometry, samples were subject to compression loading across the flat cross sectional surface. The load was applied to one end, while the other end was fixed stationary. During the simulation, each assembly was meshed into small finite elements using FEA. The results were outputted as Von Mises stresses—which is the stress at which a material will begin to yield. The Von Mises theory is often used to predict the yield point of materials under uniaxial loading conditions [38]. These stress values were compared to the yield strength of native bone (193 MPa) in order to determine the optimal shape, size, and arrangement of the HAp columns for full scaffold prototyping.

2.1.12 Fabrication and Mechanical Characterization of HAp Reinforced Scaffold

Compression testing was performed on HAp reinforced scaffolds using the Instron 5869 Mechanical Testing System, at a rate of 1 mm/min. The scaffold was fabricated as previously determined by the MoTR Lab [1,39,40,41]. Briefly, circular cross sections of electrospun poly-L-lactic acid (PLLA) were stacked to develop a cylindrical trabecular component. The outer cortical layer consisted of osteon-mimicking structures composed of electrospun PLLA [40]. They were wrapped around the trabecular assembly with 4 HAp columns inserted at positions determined by the FEA results (Figure 6). A layer of electrospun poly-D-lactic acid (PDLA) was wrapped around the scaffold to keep all of the components intact. The composite scaffold was sintered at the glass transition temperature of PDLA (55°C) for 45 minutes to bind scaffold components [39]. After all components were combined, the scaffolds were mineralized using an electrodeposition technique, previously determined by the MoTR Lab [41]. This method involved the application of an electric field, which forces ions from simulated body fluid (SBF) solution throughout the scaffold [41]. Scaffolds with and without HAp were tested to compare mechanical properties (n = 6).

Figure 6: *HAp reinforced composite trabecular and cortical bone scaffold. HAp columns marked with an **

2.1.13 Statistical Analysis

Statistical analysis was performed on all data using the ANOVA Tukey's Post Hoc test. A value of $p<0.05$ was considered statistically significant. The mean, standard deviation, and sample size were provided for all numerical data.

2.2 Results

2.2.1 Mechanical Properties

After compressive testing on an Instron 5869, data was collected for mechanical characterization. Figure 7, below, shows a sample stress strain curve that was obtained from post-sintered ceramic HAp columns. During mechanical loading, local mechanical failures, due to the propagation of structural micro and macro cracks can be seen on the curve. The slope of the longest linear region was used to calculate the compressive modulus.

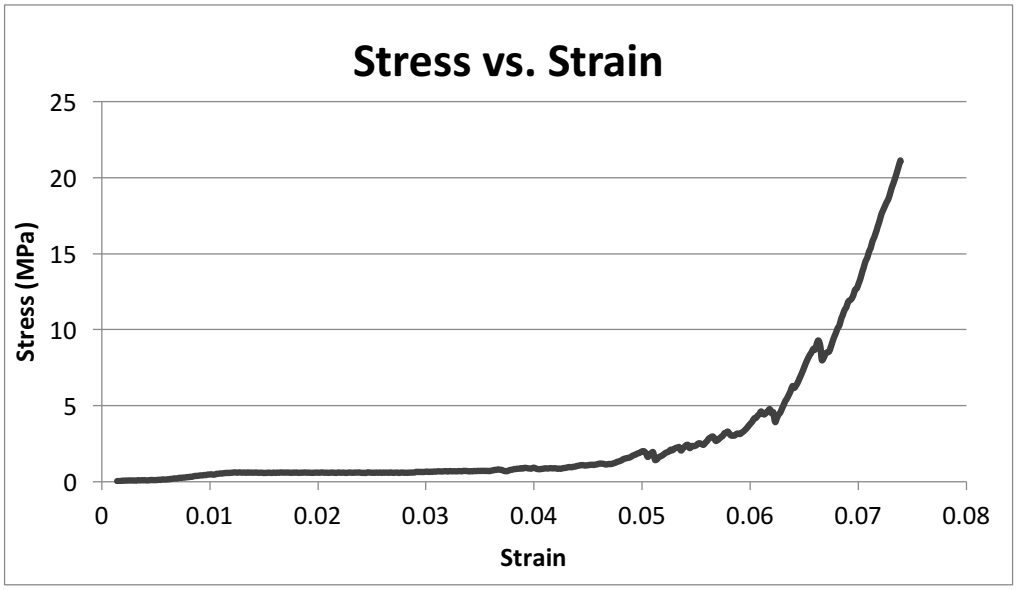

Figure 7: *Sample Stress vs. Strain curve for sintered HAp*

2.2.1.1 The Effect of Packing Pressure

The effect of increased packing pressure was assessed on columns sintered at 1200°C for 5 hours. Columns packed under 44 MPa of pressure using an Instron 5869 had a significantly higher compressive modulus. Columns fabricated under pressured conditions had a modulus of 1059 ± 215 MPa compared to a modulus of 330 ± 206 MPa

(Figure 8). Both groups had a sample size of n = 5. ANOVA Tukey's Post-Hoc Test was used to establish a p-value <0.05.

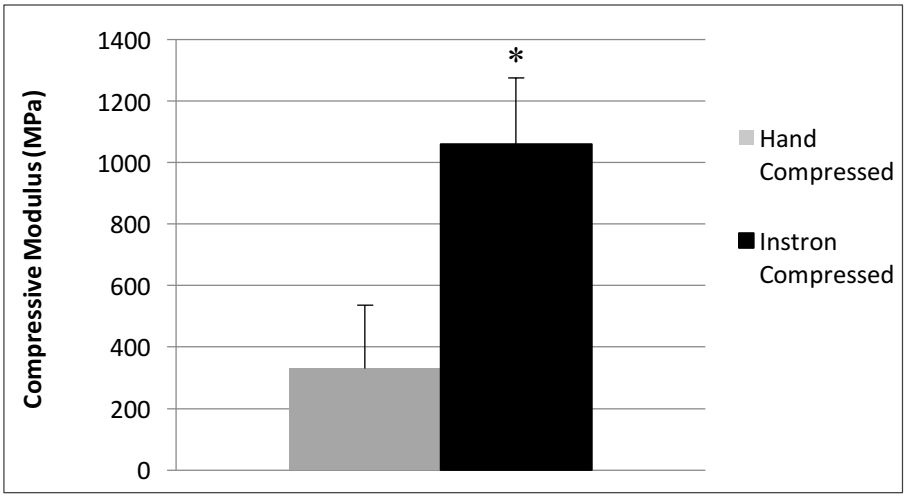

Figure 8: *Compressive modulus under various packing pressures. Sintered at 1200°C for 5 hours. ANOVA Tukey's post-hoc test: p<0.05*

2.2.1.2 The Effect of Sintering Time

Columns packed under 44 MPa of pressure were sintered at 1200°C for either 5 hours or 3 hours to assess the effect of sintering time on HAp mechanical properties. Figure 9 shows that there was a significant increase in compressive modulus when the sintering time was increased from 3 hours (475 ±198 MPa, n = 2) to 5 hours (1059 ± 215 MPa, n = 5). ANOVA Tukey's Post Hoc-Test was used to establish a p-value <0.05.

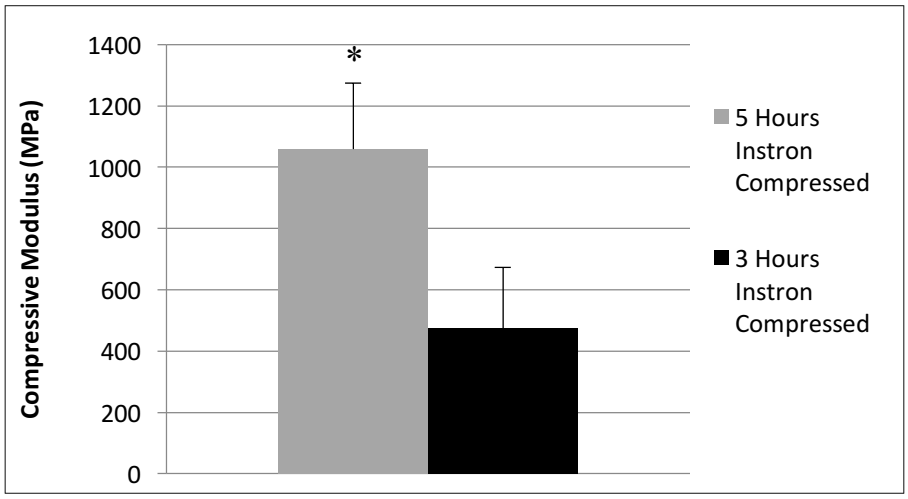

Figure 9: *Effect of varying sintering time on the compressive modulus.Packed at 44MPa and sintered at 1200°C. ANOVA Tukey's post hoc: $p<0.05$*

2.2.1.3 The Effect of Particle Size

Variance in particle size showed that nanophase HAp powder (particle size <200 nm) exhibited a significant increase in compressive modulus (1059 ± 215 MPa, n = 5) compared to reagent grade synthetic hydroxyapatite (319 ± 58 MPa, n = 5) when pressurized and sintered at 1200°C. ANOVA Tukey's Post Hoc Test was used to establish a p-value <0.0001.

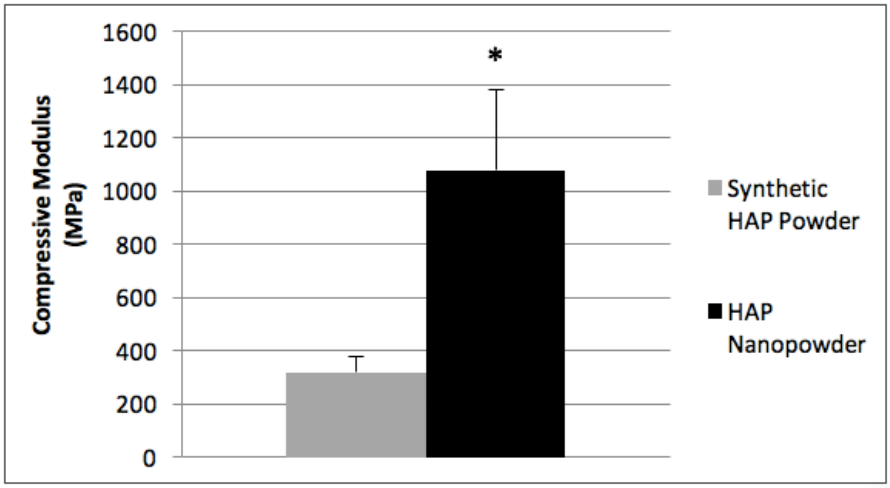

Figure 10: *Modulus of nancrystalline HAp vs reagent grade synthetic HAp Packed at 44 MPa and sintered at 1200°C for 5 hours. ANOVA Tukey's post-hoc: $p<0.0001$*

2.2.2 SEM Images of HAp Columns

SEM Images of the HAp columns were obtained to observe the effect of sintering on the formation of micro cracks within the polycrystalline structure. Columns sintered for longer times exhibited more significant surface micro cracks. The surface of columns sintered at 700°C for 3 hours can be seen in figure 11, below. While surface deformities are visible, the presence of micro cracks are minimal. Some micro cracks that can be seen are on the scale of 10 μm.

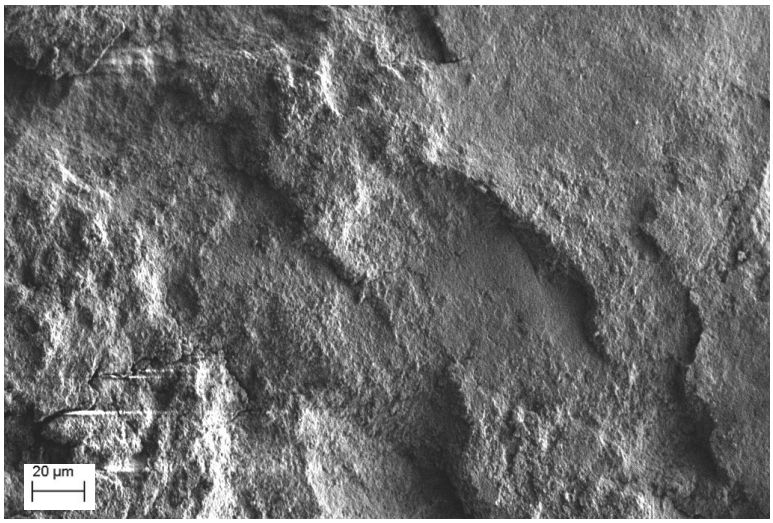

Figure 11: *Surface of HAp sintered at 700°C for 3 hours.*

When HAp was sintered at 700°C for 10 hours, significant crack formation was observed throughout the surface of the columns (Figure 12). These large-scaled cracks are on the millimeter scale and are more prominent than the micro cracks observed in figure 11.

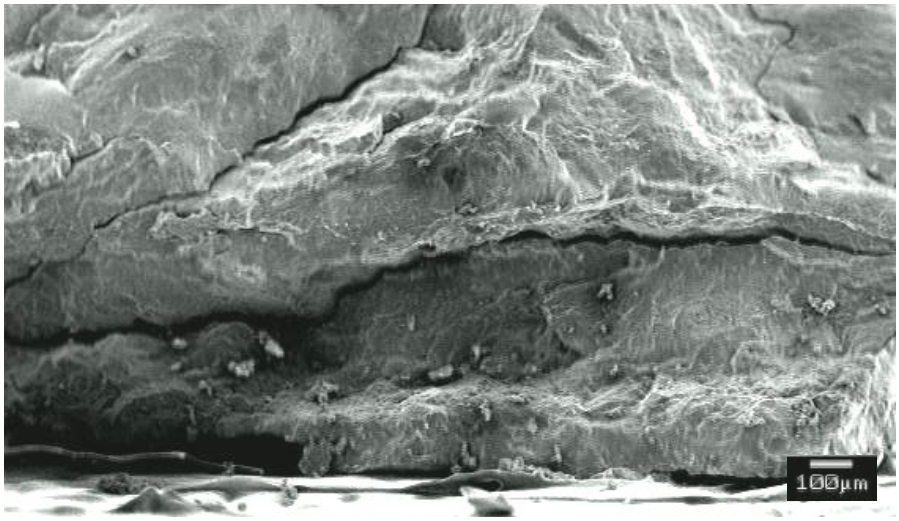

Figure 12: *Surface of HAp sintered at 700°C for 10 hours.*

For this study, columns sintered at 1200°C for 5 hours provided optimal conditions to increase mechanical properties of nanophase hydroxyapatite. Their surface was observed to be free of the large scale cracks that were seen in HAp samples sintered for 10 hours. However, surface deformities and irregularities can be seen (Figure 13).

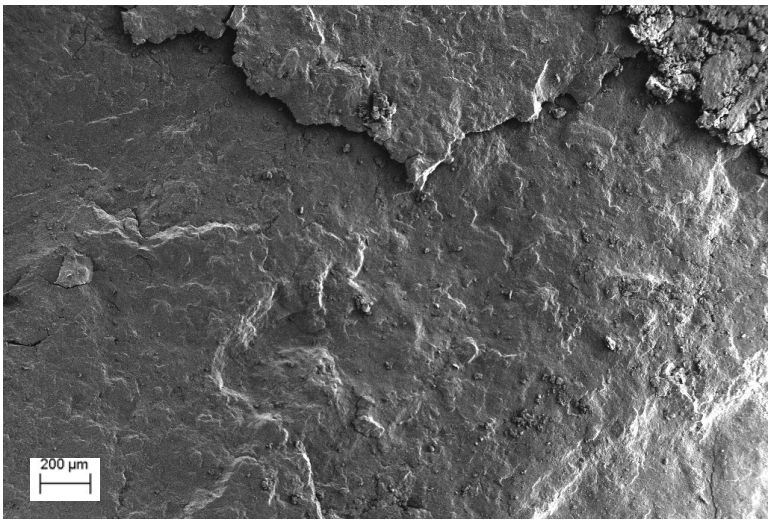

Figure 13: *Surface of HAp sintered at 1200°C for 5 hours.*

2.2.3 HAp Degradation

The degradation of sintered HAp was assessed after 4 and 6 weeks. The columns remained intact and did not exhibit any significant loss in mass or volume. The pre and post degradation structure of the columns can be seen below. Formation of black spots on the surface of the columns was observed post degradation.

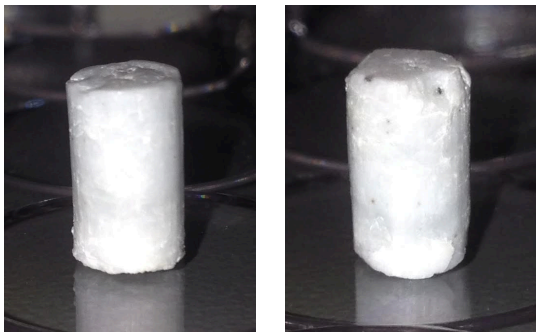

Figure 14: *One the left a HAp columns pre (left) and post (right) degradation.*

After the columns were dried in a desiccator, they were mechanically tested under the same conditions as the control; statistical analysis revealed that the columns did not experience a loss in compressive modulus. No statistical difference between the groups was detected using ANOVA. The moduli at weeks 0, 4, and 6 were 1723.46 ± 316.19 MPa, 1654.78 ± 367.41 MPa, and 1691.56 ± 818.98 MPa, respectively (Figure 15).

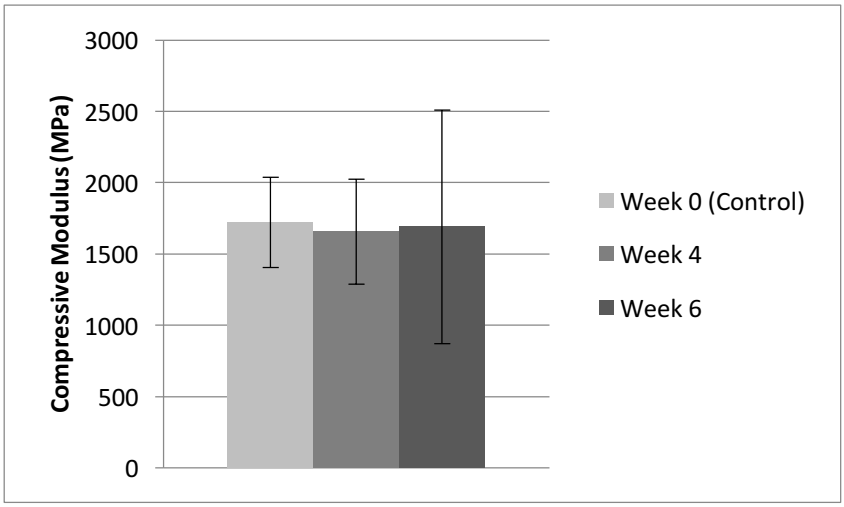

Figure 15*: 6-week degradation results of sintered HAp.*

2.2.4 Cell Viability

Cell viability was assessed using the PrestoBlue assay on days 1, 3, and 7. On Days 1 and 3, cell viability was not statistically different between control and HAp groups. By Day 7, cell viability on the HAp groups were significantly greater than the TCP control groups. In both the HAp and control groups, cell viability increased significantly over the 7-day study. Each group had a sample size of $n \geq 4$. ANOVA Tukey's Post-Hoc Test was used to establish a p-value <0.05.

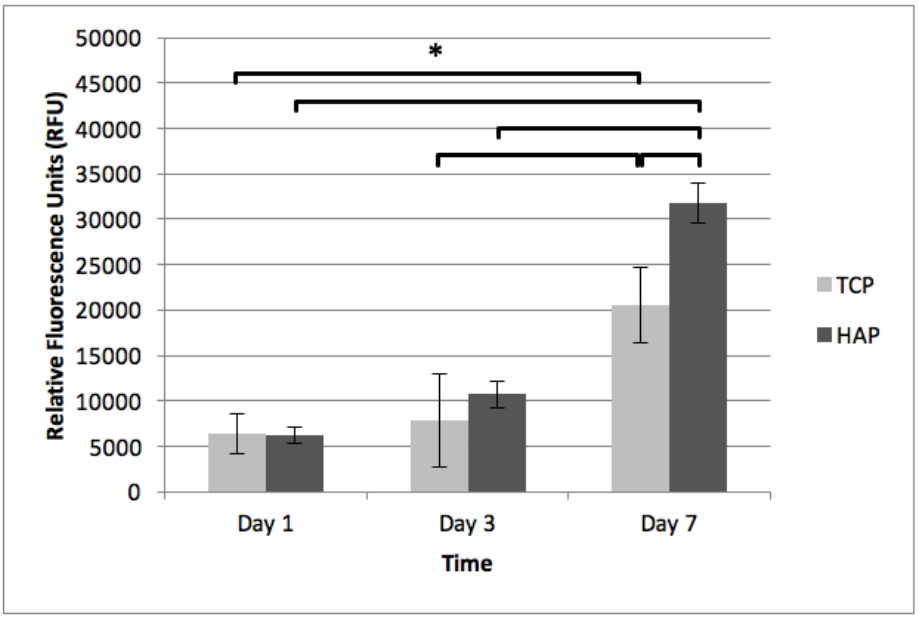

Figure 16: *Cell viability data obtained over a 1-week study using the PrestoBlue assay.*

2.2.5 Fluorescence Microscopy Images

Images of the fluorescently labeled MC3T3-E1 cells were obtained to observe cell morphology. The phalloidin labeled cytoskeletal structure can be seen in green, while the NucBlue stained nucleotides allow visualization of the nucleus in blue.

On Day 1 a distinct morphology was observed on sintered HAp groups compared to TCP. Cytoskeletal structure was observed to be have thin, linear projections on HAp groups (Figure 18) compared to the more radial shape seen on TCP control groups (Figure 17). The columns' surfaces were polished flat with sandpaper; however, cells seeded onto HAp appear to lie on multiple planes (Figure 18).

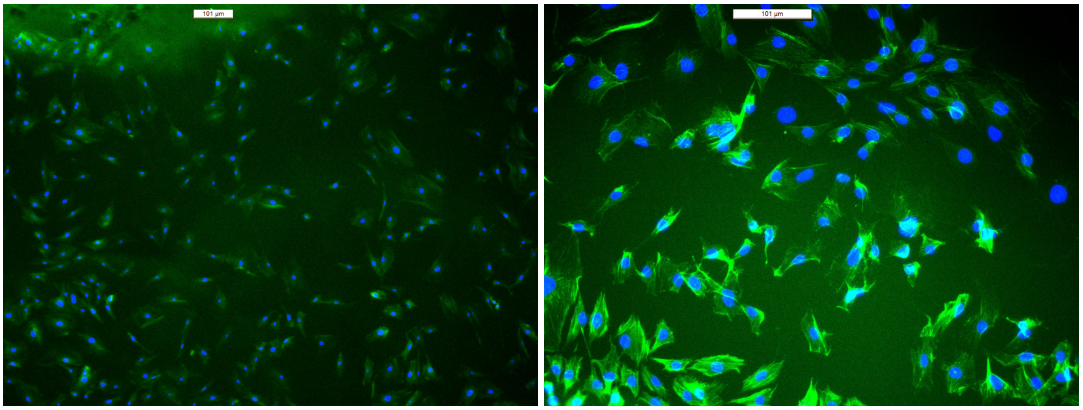

Figure 17*: MC3T3-E1 cells observed on TCP, Day 1.*

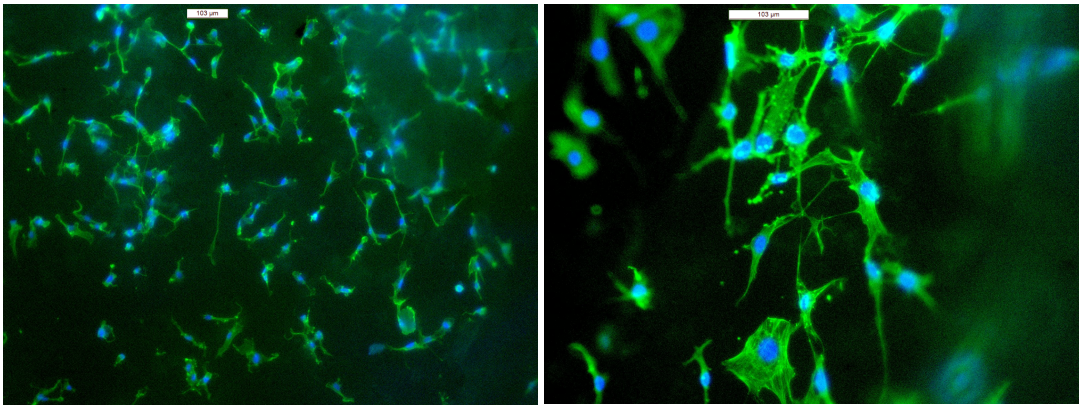

Figure 18*: MC3T3-E1 cells on sintered HAp columns, Day 1. Thin, finger-like projections can be observed.*

On Day 3, the cells appear more confluent in both the TCP control and HAp groups (Figures 19-20). A distinction in morphology remains between the groups, with cells seeded onto HAp maintaining a thin linear morphology compared to the control (Figure 20).

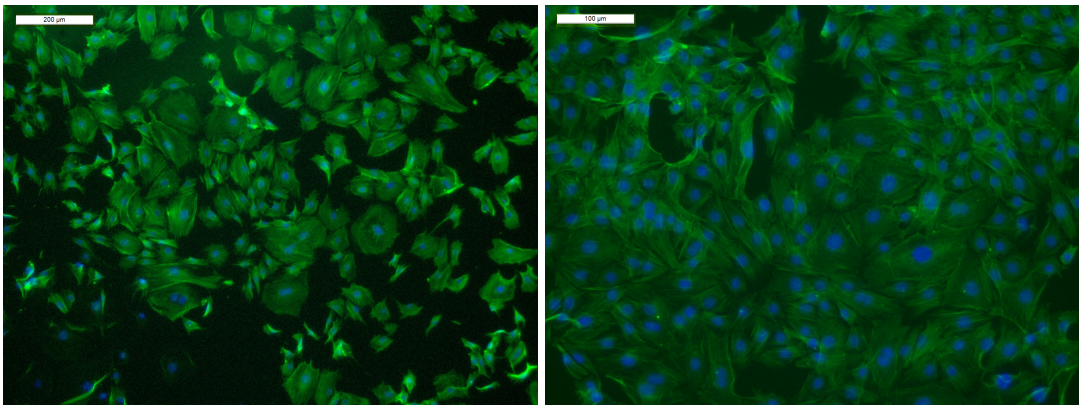

Figure 19: *MC3T3-E1 cells observed on TCP, Day 3. Cells maintained a similar morphology compared to Day 1.*

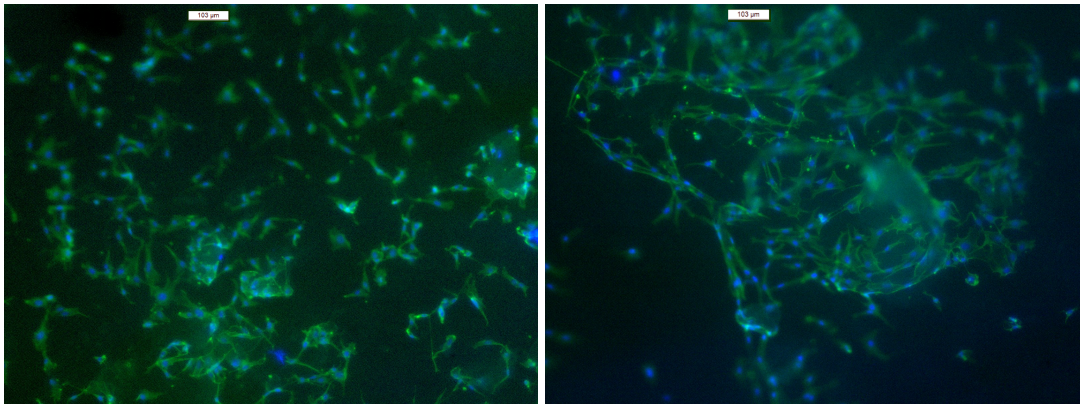

Figure 20: *MC3T3-E1 cells observed on sintered HAp, Day 3. Cells appear to have a thin, linear shape possibly guided by surface cues.*

On Day 7, the cells appear significantly more confluent compared to earlier time points. On the TCP control group, an extensive cytoskeletal network has formed, making it difficult to discern individual cell morphology (Figure 21).

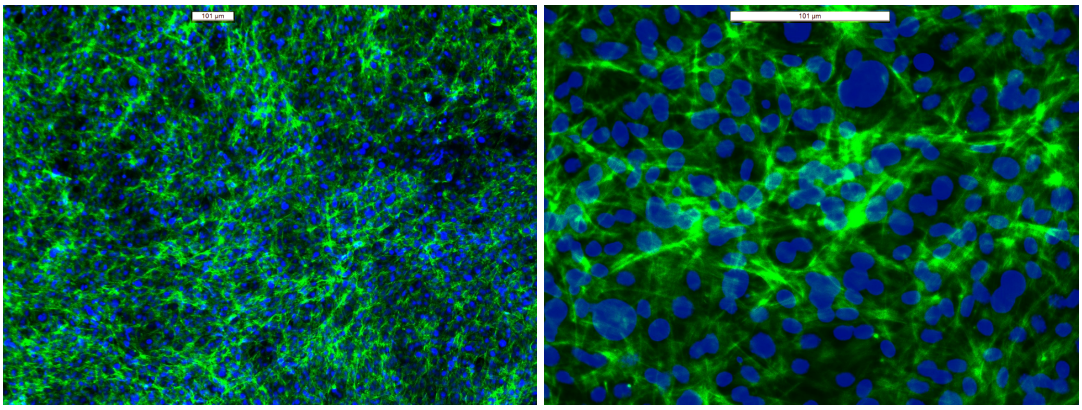

Figure 21: *MC3T3-E1 cells observed on TCP, Day 7.*

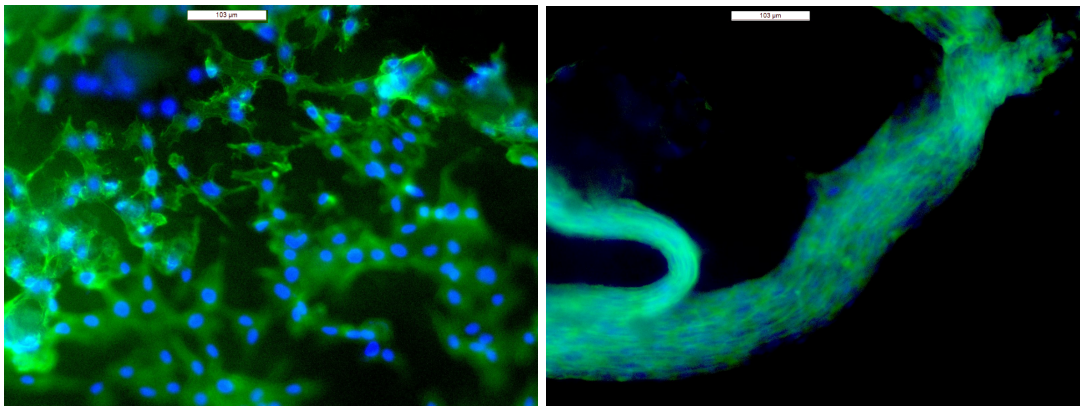

Figure 22: *MC3T3-E1 cells on HAp. On the right, cells oriented along a surface deformity or crack can be seen. Cells appear to have attached onto multiple planes throughout the HAp column.*

On The HAp groups (Figure 22), the cells could not be focused and were not clearly observable compared to earlier time points. In figure 22 it can also be seen that cells have oriented themselves along the direction of a crevice or crack on the surface of the HAp columns.

2.2.6 Scanning Electron Microscopy (SEM) Images of Cells

Cells seeded onto HAp columns appeared to be on multiple planes and were difficult to obtain focused and clear images using fluorescence microscopy. SEM imaging was used to visualize cell morphology on the surface of the HAp columns. On Day 3, linear cell projections can be seen, similar to the morphology observed using fluorescence microscopy (Figure 23).

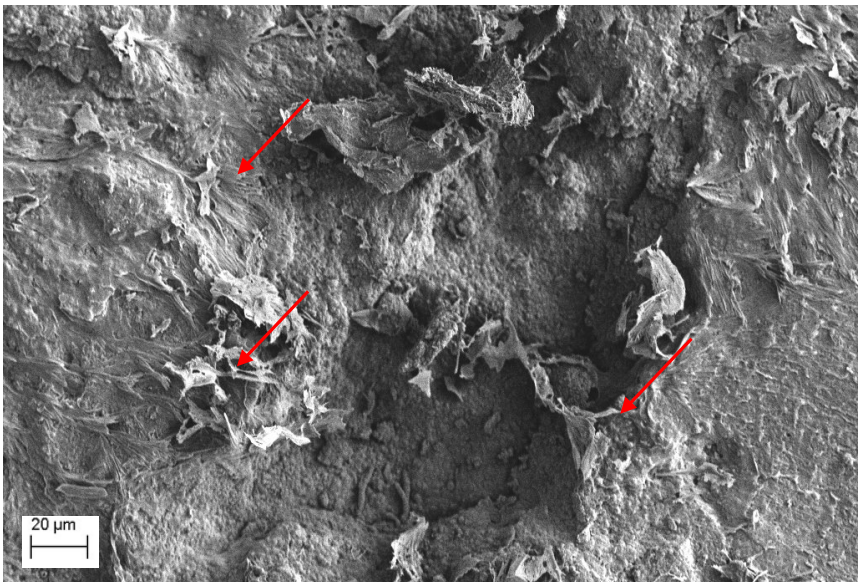

Figure 23: *SEM image of MC3T3-E1 cells on the surface of HAp, Day 3. The arrow points to a cell with finger-like projections.*

On Day 7, cells projections are more difficult to visualize. The cells appear to be covered by a layer of extracellular matrix, making visualization of cell morphology difficult (Figure 24). A visible deposition of matrix material was not observed at earlier time points in this study.

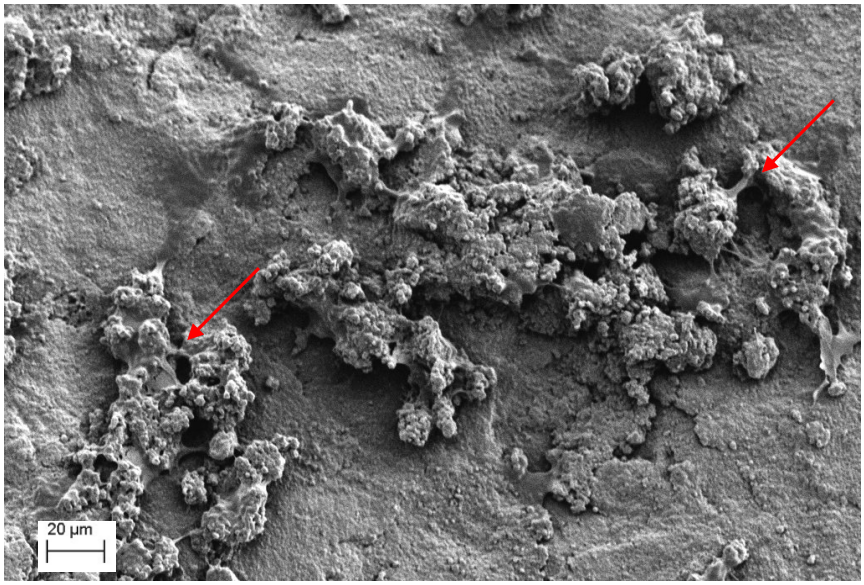

Figure 24: *SEM image of MC3T3-E1 cells on the surface of HAp, Day 7. The arrow points to a cell with visible projections surrounded by a deposited matrix layer.*

2.2.7 Finite Element Analysis to Determine Final Dimensions of the HAp Columns

Results of the FEA analysis were outputted as Von Mises Stresses, seen in figure 25. The yield strength of bone, 193 MPa, was used as the minimum criterion. Assembly 1 (four, 1 mm square columns) and assembly 3 (consisting of four, 1.5 mm cylindrical columns) satisfied this criterion, with stresses exceeding the yield strength of native whole bone. Assembly 3 (four cylindrical columns, 1.5 mm in diameter) was selected to be incorporated into the bone scaffold.

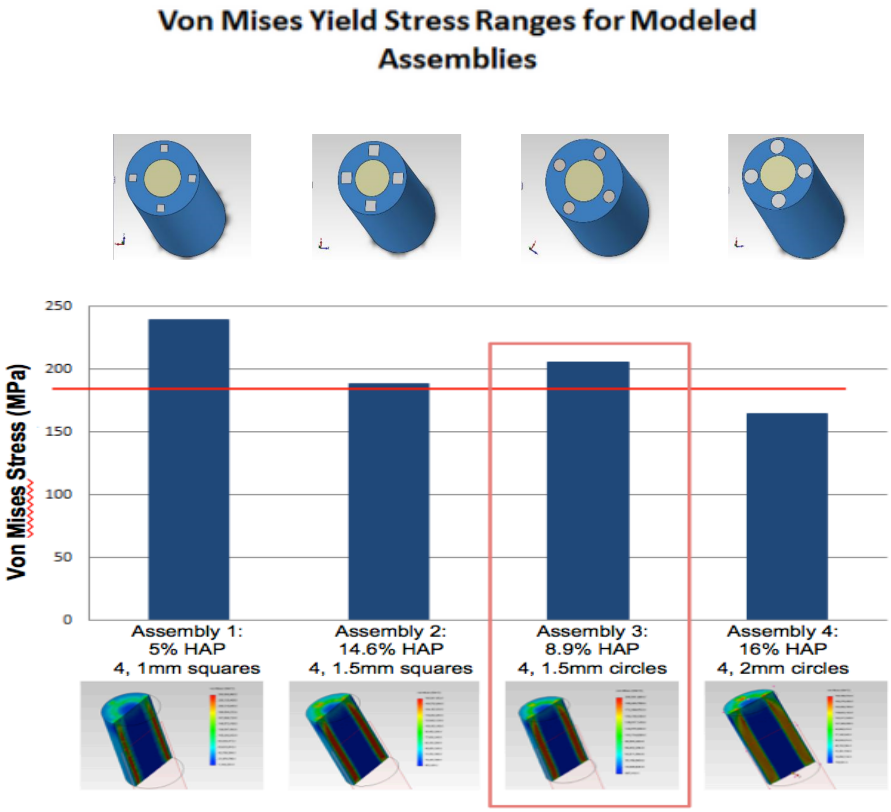

Figure 25: *Von Mises Stresses for the various assemblies tested in FEA analysis.*

The simulation showed that as the scaffold was loaded under compression, there was a higher concentration of stresses on the HAp columns. The stress distribution of the scaffold during mechanical loading can be seen in figure 26, below.

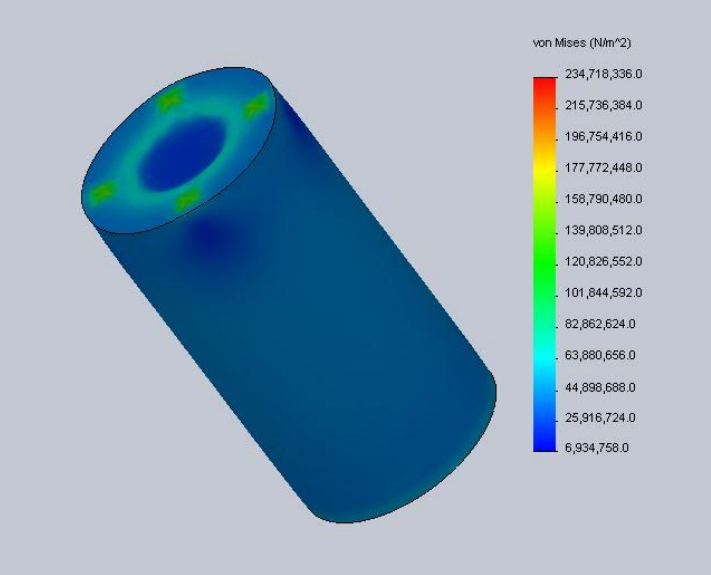

Figure 26: *Stress distribution of the scaffold. A high concentration of stress can be seen on the HAp columns along the periphery.*

2.2.8 Properties of Composite Bone Scaffold with HAp Columns

The effect of incorporating sintered HAp columns on the scaffold's compressive modulus was assessed. Scaffolds reinforced with HAp exhibited a significantly higher compressive modulus (573.61 ± 179.79 MPa) compared to scaffolds tested without HAp (350.68 ± 116.09 MPa). Scaffolds reinforced with HAp also exhibited a significantly larger ultimate compressive stress (274.71 ± 4.98 MPa) compared to scaffolds tested without HAp (157.4 ± 22.2 MPa). Both groups had a samples size of n = 6 (Figures 27-28). ANOVA Tukey's Post-Hoc Test was used to establish a p-value < 0.05.

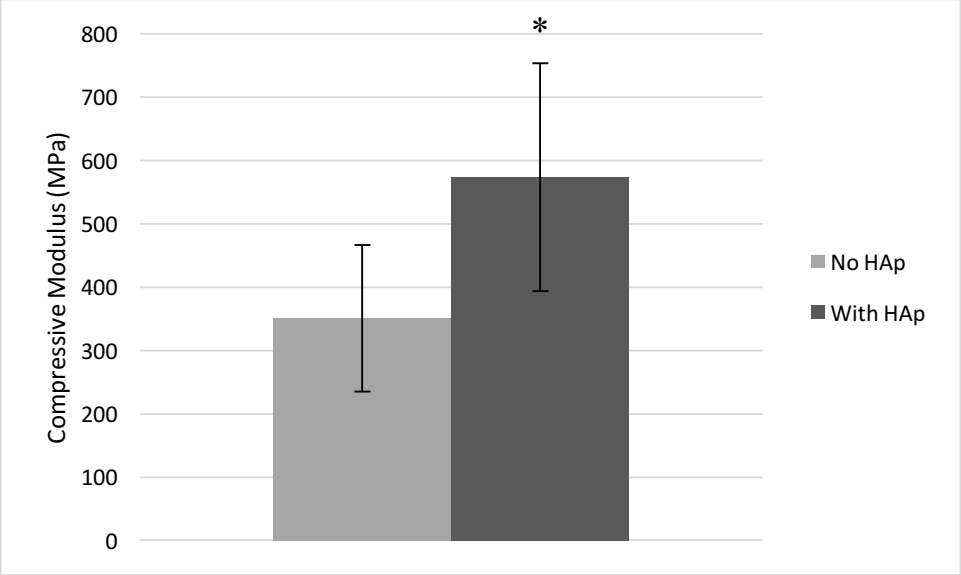

Figure 27: *Compressive modulus of HAp reinforced scaffolds vs. scaffolds without sintered HAp. ANOVA Tukey's post-hoc test: $p<0.05$*

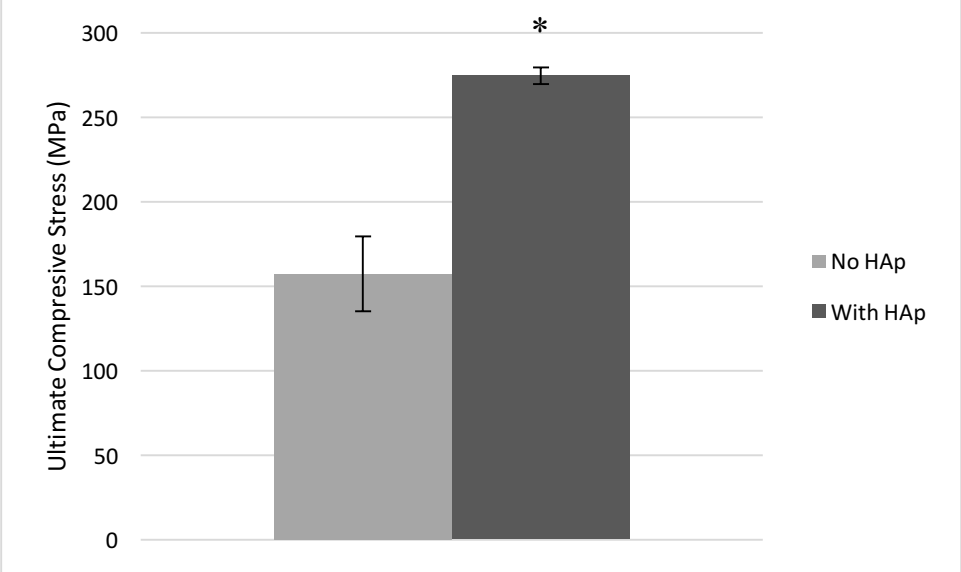

Figure 28: *Ultimate Compressive Stress (UCS) for HAp reinforced scaffolds vs. scaffolds without sintered HAp. ANOVA Tukey's post-hoc test: $p<0.05$*

2.3 Discussion

One of the challenges that persists in the field of bone tissue engineering is the design of a viable bone graft substitute that exhibits both the mechanical and biological behavior needed for successful bone regeneration. Hydroxyapatite (HAp) is a widely studied material for the development of new bone regeneration technology because of its similarity to the calcium phosphate mineral found in native bone. This project focused on the processing of HAp into viable, mechanically enhanced bioceramic columns, which can serve as a structural support system under compressive loading. Analysis of processing parameters showed that increased mechanical strength was positively correlated with densification and consolidation of HAp. This was evident in the application of high packing pressure, which resulted in a significant increase in mechanical properties. Additionally, nanophase HAp (particle size <200 nm) was shown to have a significantly higher compressive modulus than reagent grade HAp (with micro scaled particles). Sintering is another process that promotes densification of a material. It was seen that nano HAp achieved greater densification and consolidation post-sintering, compared to reagent grade HAp. Nano HAp, consequently exhibited a significantly larger compressive modulus.

	Reagent Grade HAp	HAp Nanopowder (particle size < 200nm)
Volume Decrease	12.5%	33.3%

Table 1: *Percent volume decrease of HAp packed under 44MPa of pressure, after sintering at 1200°C for 5 hours.*

Although increased density is necessary to maximize the mechanical properties of HAp, further densification under higher pressures or longer sintering times could adversely affect porosity needed for cell adhesion. While increasing sintering time—up to 5 hours—was beneficial for the maximizing the compressive modulus, sintering beyond 5 hours resulted in the formation of large-scaled cracks that can mitigate any mechanical benefits. Samples sintered at 1200°C for 5 hours exhibited surface deformities and some micro-cracks, which have been reported to have both mechanical and biological benefits. Mechanically, micro-cracks can help dissipate strain energy, increasing fracture toughness—a material property that is characteristically low for HAp [5,42]. Additionally, Shu et al. has reported that osteoblast attachment was significantly greater on HAp with induced micro-cracks compared to HAp without the presence of micro-cracks [42]. It was determined that HAp packed under 44 MPa of pressure for 10 minutes and sintered at 1200°C for 5 hours were sufficient conditions for maximizing mechanical properties of HAp under compression.

While it is known that HAp has characteristically low resorption *in vivo*, the effect of degradation on the compressive modulus of sintered nanophase HAp was unknown. Over the 6-week study, the columns did not lose any significant mass and appeared visibly intact; however, black spots were seen on the columns post-degradation. Additionally, salt deposition was seen on some of the columns, which was the result of ions from the PBS solution collecting onto the HAp columns. The compressive modulus showed no significant difference over the 6-week study. The HAp column's ability to maintain its

compressive strength throughout the study is critical in the scaffold's ability to maintain mechanical integrity throughout the process of new bone generation.

The PrestoBlue results indicate that cell viability increased for both the TCP control and HAp groups throughout the 7-day study. While there was no statistical difference in viability over the first 3 days, cells appeared more confluent in fluorescence images on day 3. The significantly higher viability on day 7 HAp groups indicates that cells are able to attach and proliferate on the columns, despite minimal porosity on the dense bioceramic material. Prior to seeding, the HAp columns were soaked in media overnight, which could promote cell attachment via interactions with HAp-adhered growth factors and proteins from the serum supplemented media. Additionally, the presence of surface deformities such as crevices and micro-cracks provide attachment points and topological cues for the cells. Studies have shown that the presence of micro-cracks can enhance osteoblast attachment and alignment along the direction of micro cracks [42]. On day 7, fluorescence microscopy showed MC3T3-E1 cells attaching and aligning along what appears to be a crack on the surface of HAp (Figure 22). Despite the lack of large pores on the dense HAp material, the cells appear to have found crevices and cracks in order to penetrate the HAp surface and attach on multiple planes of the column. This is evidenced by a few out of focus cells seen in the fluorescence images of HAp groups. By Day 7, a deposited matrix layer covered the cells, making it difficult to visualize them using fluorescence microscopy. Blurry images seen in figure 22 could be the result of light scattering from the matrix layer. The deposited matrix was observed using SEM on day 7 HAp groups. The presence of ascorbic acid in the cell culture media used for the study in

known to promote osteoblastic differentiation of the preostoblastic MC3T3-E1 (subclone 4) cells. Shu et al. reported that osteoblast activity and gene expression was up-regulated by the presence of surface micro-cracks and greater mineralization was observed at these sites [42]. Additionally, external cues such as the dissolution of calcium ions released from the surface of HAp could contribute to the osteoblast activity.

The FEA results showed that the Von Mises stresses of assemblies 1 and 3 were sufficiently higher than the yield strength of bone (193 MPa). Although assembly 1 had a higher Von Mises Stress, the limitations of handling HAp and the difficulty of fabricating square columns under large packing pressures were considered. Assembly 3 (consisting of four, 1.5mm cylindrical columns) was selected. The preliminary mechanical data showed a significant increase in the compressive modulus of the HAp reinforced bone scaffold. Although the compressive modulus does not match that of native bone, the ultimate compressive stress increased significantly to a value larger than that of native bone (193 MPa). Furthermore, the scaffolds were mineralized using electrodeposition, a technique that may have led to the degradation of the PLA polymer, thereby limiting the mechanical advantages of HAp incorporation. In this preliminary study, the ability for sintered HAp to serve as a support system under compressive loads was further confirmed by the concentration of stresses on the HAp columns seen during the simulation (Figure 26). This minimizes the shear stresses at the interface between various components of the 3-D scaffold. Scaffold shearing can negatively impact its structural and mechanical integrity leading to premature failure.

CHAPTER 3 – Conclusions and Future Works

In this study a polymeric composite trabecular and cortical 3-D bone scaffold was successfully reinforced with sintered HAp columns. During the initial characterization of the HAp reinforced scaffold, the overall mechanical properties were improved with the incorporation of HAp; however, additional processing modifications need to be made to match the load-bearing capabilities of native bone tissue. The incorporation of additional HAp columns could be necessary to maximize load-bearing ability. Because HAp has a characteristically slow resorption rate, the effect of incorporating other calcium phosphates, such as beta tricalcium phosphate needs to be assessed. Processing parameters (sintering time and temperature, packing pressure, etc.) may need to be modified for the composite column. Additionally, different mineralization techniques need to be assessed to prevent PLA polymer degradation and improve the overall mechanical properties of the scaffold. In the future additional forms of mechanical testing need to be performed on the scaffold. Under physiological conditions, bone experiences a combination of loads including tension, torsion, and bending. Torsion and bending tests need to be performed in order to obtain a more thorough mechanical evaluation of the scaffold. For example, under torsion, properties at the interfaces of the various scaffold components will be affected.

A more thorough biological analysis of the extracellular matrix secreted by the MC3T3-E1 cells can be performed. Levels of osteocalcin could be detected to determine the differentiation state of the murine preosteoblast cells over the 7-day period. In the future,

the scaffold's *in vivo* response needs to be assessed in an animal model to determine biocompatibility and degradation. Extensive *in vivo* testing is required to ultimately determine the scaffold's ability to serve as a viable bone graft substitute and promote the generation of new bone tissue. However, before the scaffold can be applied in clinical practice, considerations need to be made concerning how it will be sterilized and how these techniques may affect the mechanical and biological properties of the scaffold.

REFERENCES

[1] Andric, T., Wright, L. D., Taylor, B. L., & Freeman, J. W. (2012). Fabrication and characterization of three-dimensional electrospun scaffolds for bone tissue engineering. Journal of Biomedical Materials Research Part A, 100A(8), 2097-2105.

[2] . Hing KA. Bone repair in the twenty-first century: Biology, chemistry or engineering? Philos Trans A Math Phys Eng Sci 2004;362: 2821–2850.

[3] Rho, J., Kuhn-Spearing, L., & Zioupos, P. (1998). Mechanical properties and the hierarchical structure of bone. Medical Engineering & Physics, 20(2), 92-102.

[4] Boskey, A. L. (2013). Bone composition: Relationship to bone fragility and antiosteoporotic drug effects. BoneKEy Rep, 2, Article number: 447

[5] Suchanek, W., & Yoshimura, M. (1998). Processing and properties of hydroxyapatite-based biomaterials for use as hard tissue replacement implants. Journal of Materials Research, 13(1), 94–117

[6] Sharir, A., Barak, M. M., & Shahar, R. (2008). Whole bone mechanics and mechanical testing. The Veterinary Journal, 177(1), 8-17.

[7] Cole, J. H., & van, d. M. (2011). Whole bone mechanics and bone quality. Clinical Orthopaedics and Related Research®, 469(8), 2139-2149.

[8] Gong, J. K., Arnold, J. S., & Cohn, S. H. (1964). Composition of trabecular and cortical bone. The Anatomical Record, 149(3), 325-331.

[9] Viguet-Carrin, S., Garnero, P., & Delmas, P. D. (2006). The role of collagen in bone strength. Osteoporosis International : A Journal Established as Result of Cooperation between the European Foundation for Osteoporosis and the National Osteoporosis Foundation of the USA, 17(3), 319-336.

[10] Wopenka, B., & Pasteris, J. D. (2005). A mineralogical perspective on the apatite in bone. Materials Science and Engineering: C, 25(2), 131-143.

[11] Rehman, I., & Bonfield, W. (1997). Characterization of hydroxyapatite and carbonated apatite by photo acoustic FTIR spectroscopy. Journal of Materials Science: Materials in Medicine, 8(1), 1-4.

[12] Keaveny TM, Hayes WC. (1993) Mechanical properties of cortical and trabecular bone. Bone A. 7:285–344.

[13] Victoria, G., Petrisor, B., Drew, B., & Dick, D. (2009). Bone stimulation for fracture healing: What's all the fuss? Indian Journal of Orthopaedics, 43(2), 117-120.

[14] Musculoskeletal injuries report: Incidence, risk factors and prevention. Rosemon, IL: American Academy of Orthopaedic Surgeons; 2000.

[15] Einhorn, T. A., & Gerstenfeld, L. C. (2015). Fracture healing: Mechanisms and interventions. Nat Rev Rheumatol, 11(1), 45-54.

[16] Hernandez, C. J. (2013). Bone fatigue, stress fractures and bone repair (sun valley 2013). IBMS Bonekey, 10, Article number: 448

[17] Office of the Surgeon General (US). Bone Health and Osteoporosis: A Report of the Surgeon General. Rockville (MD): Office of the Surgeon General (US); 2004. 4, The Frequency of Bone Disease.

[18] Ganesh, V. K., Ramakrishna, K., & Ghista, D. N. (2005). Biomechanics of bone-fracture fixation by stiffness-graded plates in comparison with stainless-steel plates. BioMedical Engineering OnLine, 4, 46-46.

[19] Giannoudis, P. V., Dinopoulos, H., & Tsiridis, E. (2005) Bone substitutes: An update. Injury, 36(3), S20-S27.

[20] Bohner, M., Galea, L., & Doebelin, N. (2012). Calcium phosphate bone graft substitutes: Failures and hopes. Journal of the European Ceramic Society, 32(11), 2663-2671.

[21] Kurien, T., Pearson, R. G., & Scammell, B. E. (2013). Bone graft substitutes currently available in orthopaedic practice. Bone & Joint Journal, 95-B(5), 583-597. doi:10.1302/0301-620X.95B5.30286

[22] Myeroff, C., & Archdeacon, M. (2011). Autogenous bone graft: Donor sites and techniques. The Journal of Bone & Joint Surgery, 93(23), 2227-2236. doi:10.2106/JBJS.J.01513

[23] Bos, G. D., Goldberg, V. M., Zika, J. M., Heiple, K. G., & Powell, A. E. (1983). Immune responses of rats to frozen bone allografts. The Journal of Bone & Joint Surgery, 65(2), 239-246.

[24] Ross, L. T. (2000). Heterotopic bone formation causing recurrent donor site pain following iliac crest bone harvesting. British Journal of Neurosurgery, 14(5), 476-479.

[25] Boyce T, Edwards J, Scarborough N. (1999) Allograft bone: the influence of processing on safety and performance. Orthop Clin North Am; (4):571-81

[26] Lord, C. F., Gebhardt, M. C., Tomford, W. W., & Mankin, H. J. (1988). Infection in bone allografts. incidence, nature, and treatment. The Journal of Bone & Joint Surgery, 70(3), 369-376.

[27] Wheeler, D. L., & Enneking, W. F. (2005). Allograft bone decreases in strength in vivo over time. Clinical Orthopaedics and Related Research, 435

[28] Nguyen, H., Morgan, D. A. F., & Forwood, M. R. (2007). Sterilization of allograft bone: Effects of gamma irradiation on allograft biology and biomechanics. Cell and Tissue Banking, 8(2), 93-105.

[29] Liu, J., & Kerns, D. G. (2014). Mechanisms of guided bone regeneration: A review. The Open Dentistry Journal, 8, 56-65.

[30] Nazirkar, G., Singh, S., Dole, V., & Nikam, A. (2014). Effortless effort in bone regeneration: A review. Journal of International Oral Health : JIOH, 6(3), 120-124.

[31] Bohner, M. (2010). Resorbable biomaterials as bone graft substitutes. Materials Today, 13(1–2), 24-30.

[32] Rahaman, M. N., Day, D. E., Sonny Bal, B., Fu, Q., Jung, S. B., Bonewald, L. F., et al. (2011). Bioactive glass in tissue engineering. Acta Biomaterialia, 7(6), 2355-2373.

[33] Nandi, S., Roy, S., Mukherjee, P., Kundu, B., De, D., & Basu, D. (2010). - Orthopaedic applications of bone graft & graft substitutes : A review. Indian Journal of Medical Research, 132(7), 15-30

[34] Fu, Q., Saiz, E., Rahaman, M. N., & Tomsia, A. P. (2011). Bioactive glass scaffolds for bone tissue engineering: State of the art and future perspectives. Materials Science & Engineering.C, Materials for Biological Applications, 31(7), 1245-1256.

[35] Saikia, K., Bhattacharya, T., Bhuyan, S., Talukdar, D., Saikia, S., & Jitesh, P. Calcium phosphate ceramics as bone graft substitutes in filling bone tumor defects. (2008) Indian J Orthop, 42(2), 169-172.

[36] Moore, W. R., Graves, S. E., & Bain, G. I. (2001). Synthetic bone graft substitutes. ANZ Journal of Surgery, 71(6), 354-361.

[37] Damien, C. J., & Parsons, J. R. (1991). Bone graft and bone graft substitutes: A review of current technology and applications. Journal of Applied Biomaterials, 2(3), 187-208.

[38] Raghava, R., Caddell, R. M., & Yeh, G. S. Y. (1973). The macroscopic yield behaviour of polymers. Journal of Materials Science, 8(2), 225-232.

[39] Taylor, B. L., Limaye, A., Yarborough, J., & Freeman, J. W. (2016). Investigating processing techniques for bovine gelatin electrospun scaffolds for bone tissue regeneration. Journal of Biomedical Materials Research Part B: Applied Biomaterials, , n/a-n/a

[40] Andric, T., Sampson, A. C., & Freeman, J. W. (2011). Fabrication and characterization of electrospun osteon mimicking scaffolds for bone tissue engineering. Materials Science and Engineering: C, 31(1), 2-8.

[41] Taylor BL. The development and characterization of an osteoinductive pre-vascularized
scaffold for bone tissue regeneration. New Brunswick, NJ: Rutgers University; 2016.

[42] Shu, Y., Baumann, M. J., Case, E. D., Irwin, R. K., Meyer, S. E., Pearson, C. S., et al. (2014). Surface microcracks signal osteoblasts to regulate alignment and bone formation. Materials Science & Engineering.C, Materials for Biological Applications, 0, 191-200.